

Erasure Thresholds for Hyperbolic and Semi-Hyperbolic Surface Codes

Aygul Azatovna Galimova¹

¹*Department of Mathematics
Duke University, Durham, NC 27708, USA*

Abstract

We extend the circuit-level erasure noise model and Wang et al. quadratic expansion fitting of Chang et al. from planar surface codes to hyperbolic CSS surface codes. Under Chang et al.'s noise models, the $\{8, 3\}$ Bolza fine-grained family threshold reaches 3.6% under the general-Pauli models (which coincide at temporal resolution $\eta = 1$) and 4.7% under the tailored spatially perfect model at $R_e = 1$ (pure erasure). The corresponding erasure-to-Pauli ratios ($5.0\times$ and $6.5\times$) match the surface code values to within 5%. Per-observable crossing-point analysis at $R_e = 1$ (Models 1–3) independently yields an erasure-to-Pauli ratio of $5.3\times$. These results establish that the erasure advantage extends to hyperbolic codes.

Contents

1	Introduction	3
2	Background	4
2.1	The Stabilizer Formalism	4
2.2	Hyperbolic Geometry and Tessellations	4
2.2.1	The Poincaré Disk Model	4
2.2.2	Fuchsian Groups and Quotient Surfaces	5
2.2.3	Schläfli Symbols and Tessellations	5
2.2.4	Quotient Surfaces and Combinatorial Parameters	5
2.2.5	Asymptotic Scaling	6
2.3	Hyperbolic Surface Codes	8
3	Methods	8
3.1	Code Construction	8
3.1.1	Wythoff Construction and Triangle Groups	8
3.1.2	LINS Algorithm and Face 3-Coloring	9
3.1.3	Code Parameters	9
3.2	Fine-Graining	9
3.2.1	Procedure	9
3.2.2	Geometric Construction	9
3.2.3	Color Inheritance	10
3.3	Syndrome Extraction Circuit	10
3.4	Pauli Noise Model	11
3.5	Erasure Noise Model	11

3.6	Phenomenological Noise Model	12
3.7	Decoder	12
3.8	Threshold Estimates	12
4	Results	12
4.1	Base Code Results	12
4.1.1	Threshold vs. Erasure Fraction	13
4.2	Fine-Grained Code Results	14
4.3	Statistical Uncertainty	15
5	Discussion	19
5.1	Comparison with the Literature	19
5.2	Surface Code Validation	19
6	Conclusion	20
A	Results for $\{10, 3\}$ and $\{12, 3\}$ Families	22

1 Introduction

Quantum error correction (QEC) protects logical quantum information by encoding it redundantly across many physical qubits. QEC performance depends on the noise model. Matching the decoder to the noise structure can improve thresholds and reduce qubit overhead. Erasure noise—in which error locations are known to the decoder—is one such structured model, and several hardware platforms now support detecting error locations before decoding.

Physical systems that convert leakage or photon loss into detectable erasure events include dual-rail photonic qubits [4], alkaline-earth Rydberg atoms [5], and superconducting circuits with metastable states [6, 7]. When the decoder knows which qubits have been corrupted, it can restrict its search to the erased locations. The resulting thresholds are several times higher than under standard Pauli noise.

For the toric code under code-capacity noise, the erasure threshold is 50% and the depolarizing threshold is $\sim 10.9\%$: a ratio of $\sim 4.6\times$ [8, 9]. For the planar surface code under circuit-level noise, Chang et al. report erasure thresholds of $\sim 4.2\%$ – 6.0% depending on the erasure check model (imperfect vs. perfect, general vs. tailored decoding). The corresponding Pauli threshold is $\sim 1.0\%$; the resulting ratios are 4.2 – $6.0\times$ [7]. Across codes and noise models, erasure thresholds consistently exceed Pauli thresholds by a factor of 4 – $5\times$.

Hyperbolic surface codes encode $k = \Theta(n)$ logical qubits into n physical qubits on tessellations of closed hyperbolic surfaces, with constant encoding rate and logarithmic distance $d = O(\log n)$ [10, 17]. In the CSS formulation, Breuckmann and Terhal [10] establish code-capacity Pauli thresholds. Breuckmann et al. [11] report a $\sim 1.3\%$ phenomenological threshold for $\{4, 5\}$ codes and introduce semi-hyperbolic codes via lattice subdivision. In the Floquet formulation, Fahimniya et al. [12] report phenomenological thresholds of $\sim 0.1\%$ on $\{8, 3\}$ tilings, and Higgott and Breuckmann [13] achieve ~ 1.5 – 2% under circuit-level depolarizing noise (SD6).

No prior work reports circuit-level thresholds—Pauli or erasure—for $\{p, 3\}$ CSS hyperbolic surface codes. We construct 14 such codes across three tessellation families ($\{8, 3\}$, $\{10, 3\}$, $\{12, 3\}$) and 11 semi-hyperbolic (fine-grained) codes via the Wythoff kaleidoscopic construction with the LINS algorithm [14, 16]. We focus on the $\{8, 3\}$ Bolza family, which forms a proper scaling family with increasing distance under fine-graining. Results for the $\{10, 3\}$ and $\{12, 3\}$ families are reported in Appendix A.

The main findings are:

1. The $\{8, 3\}$ base codes (6 codes, $n = 48$ – 648) achieve Pauli pseudothresholds of 0.24 – 0.49% , increasing with code size. Under erasure noise, three codes have measurable pseudothresholds of 3.3 – 3.7% ; the remainder exceed the tested range.
2. The Bolza fine-grained family (H16, $f = 2$ – 4) achieves Pauli pseudothresholds up to 0.63% and erasure pseudothresholds up to 4.4% . At $R_e = 1$ (Models 1–3), the per-observable family threshold gives an erasure-to-Pauli ratio of $5.3\times$ (Table 6), comparable to the 4.2 – $5.6\times$ reported for planar surface codes [7].
3. Under Chang et al.’s erasure noise model, the Bolza family threshold reaches 3.6% (Models 1–3) and 4.7% (Model 4) at $R_e = 1$. The erasure-to-Pauli ratios ($5.0\times$ and $6.5\times$) match the surface code values to within 5% .

2 Background

2.1 The Stabilizer Formalism

The stabilizer formalism [1] provides a group-theoretic framework for quantum error correction. For n qubits, the Pauli group is $\mathcal{P}_n = \{\pm 1, \pm i\} \times \{I, X, Y, Z\}^{\otimes n}$.

Definition 1 (Stabilizer Code). An $[[n, k, d]]$ stabilizer code is a 2^k -dimensional subspace of $(\mathbb{C}^2)^{\otimes n}$ determined by an abelian subgroup $\mathcal{S} \subseteq \mathcal{P}_n$:

$$\mathcal{C} = \{|\psi\rangle \in (\mathbb{C}^2)^{\otimes n} : g|\psi\rangle = |\psi\rangle \text{ for all } g \in \mathcal{S}\}, \quad (1)$$

where \mathcal{S} does not contain $-I$, $|\mathcal{S}| = 2^{n-k}$, and $\mathcal{S} = \langle g_1, \dots, g_{n-k} \rangle$.

Definition 2 (Logical Operators). Logical operators are elements of the normalizer modulo the stabilizer:

$$\text{Logicals} = N(\mathcal{S})/\mathcal{S}, \quad (2)$$

where $N(\mathcal{S}) = \{P \in \mathcal{P}_n : PgP^{-1} \in \mathcal{S} \text{ for all } g \in \mathcal{S}\}$.

Definition 3 (Code Distance). The distance of a stabilizer code is:

$$d = \min\{\text{wt}(L) : L \in N(\mathcal{S}) \setminus \mathcal{S}\}, \quad (3)$$

where $\text{wt}(L)$ is the number of non-identity tensor factors of the Pauli operator L .

Definition 4 (CSS Code). A Calderbank-Shor-Steane (CSS) code [2, 3] is a stabilizer code whose generators partition into X -type (products of X only) and Z -type (products of Z only). The code is specified by two binary parity-check matrices $H_X \in \mathbb{F}_2^{r_X \times n}$ and $H_Z \in \mathbb{F}_2^{r_Z \times n}$, where each row of H_X defines an X -stabilizer generator and each row of H_Z defines a Z -stabilizer generator. For these to commute, the matrices must satisfy

$$H_X H_Z^T = 0 \quad \text{over } \mathbb{F}_2. \quad (4)$$

The number of encoded logical qubits is $k = n - \text{rank}(H_X) - \text{rank}(H_Z)$, and the code distance is $d = \min(d_X, d_Z)$, where d_X is the minimum weight of a nontrivial X -logical operator and d_Z is defined analogously.

2.2 Hyperbolic Geometry and Tessellations

2.2.1 The Poincaré Disk Model

The hyperbolic plane \mathbb{H}^2 is a two-dimensional Riemannian manifold with constant negative Gaussian curvature $K = -1$. In the Poincaré disk model $\mathbb{D} = \{z \in \mathbb{C} : |z| < 1\}$, the metric is:

$$ds^2 = \frac{4|dz|^2}{(1 - |z|^2)^2}. \quad (5)$$

The distance between two points $z_1, z_2 \in \mathbb{D}$ is:

$$\text{dist}(z_1, z_2) = 2 \operatorname{arctanh} \left(\frac{|z_1 - z_2|}{|1 - z_1 \bar{z}_2|} \right). \quad (6)$$

The isometries of \mathbb{D} are Möbius transformations in $\text{PSU}(1, 1)$. These transformations preserve hyperbolic distances but distort Euclidean lengths.

2.2.2 Fuchsian Groups and Quotient Surfaces

A Fuchsian group is a discrete subgroup of $\mathrm{PSL}(2, \mathbb{R})$, the group of orientation-preserving isometries of \mathbb{H}^2 . Each Fuchsian group Γ has a fundamental domain $\mathcal{F} \subset \mathbb{H}^2$ such that translates of \mathcal{F} tile the hyperbolic plane.

Definition 5 (Fundamental Domain). A fundamental domain for a Fuchsian group Γ is a connected region $\mathcal{F} \subset \mathbb{H}^2$ such that:

1. $\bigcup_{\gamma \in \Gamma} \gamma(\mathcal{F}) = \mathbb{H}^2$ (the translates cover the plane),
2. $\gamma_1(\mathcal{F})^\circ \cap \gamma_2(\mathcal{F})^\circ = \emptyset$ for $\gamma_1 \neq \gamma_2$ (interiors are disjoint).

When Γ is torsion-free (no elements of finite order except identity), the quotient \mathbb{H}^2/Γ is a closed orientable surface of genus $g \geq 2$. The genus is determined by the hyperbolic area of the fundamental domain via the Gauss-Bonnet theorem:

$$\mathrm{Area}(\mathcal{F}) = 2\pi(2g - 2) = -2\pi\chi, \quad (7)$$

where $\chi = 2 - 2g$ is the Euler characteristic.

2.2.3 Schläfli Symbols and Tessellations

Definition 6 (Schläfli Symbol). A $\{p, q\}$ tessellation is a regular tiling where each face is a regular p -gon and each vertex has degree q .

Theorem 1 (Hyperbolic Condition). A $\{p, q\}$ tessellation exists in the hyperbolic plane if and only if:

$$(p - 2)(q - 2) > 4. \quad (8)$$

Equivalently: $\frac{1}{p} + \frac{1}{q} < \frac{1}{2}$.

For our code families:

- $\{8, 3\}$: $(8 - 2)(3 - 2) = 6 > 4$.
- $\{10, 3\}$: $(10 - 2)(3 - 2) = 8 > 4$.
- $\{12, 3\}$: $(12 - 2)(3 - 2) = 10 > 4$.

To obtain finite codes, we find a torsion-free normal subgroup $\Gamma \subset \Delta(p, q, 2)$ of the triangle group. The finite quotient $\Delta(p, q, 2)/\Gamma$ defines a tiling of the closed surface \mathbb{H}^2/Γ with V vertices, E edges, and F faces [13].

2.2.4 Quotient Surfaces and Combinatorial Parameters

A closed hyperbolic surface Σ_g of genus $g \geq 2$ is realized as a quotient \mathbb{H}^2/Γ , where Γ is a discrete, torsion-free Fuchsian group. The Euler characteristic relates the cell counts:

$$\chi = V - E + F = 2 - 2g. \quad (9)$$

Proposition 1 (Combinatorial Parameters). For a uniform $\{p, q\}$ tessellation of a genus- g surface (all faces are p -gons, all vertices have degree q), the constraints $qV = 2E = pF$ yield:

$$F = \frac{4q(g - 1)}{pq - 2p - 2q}, \quad E = \frac{pF}{2}, \quad V = \frac{pF}{q}. \quad (10)$$

Example 1 (Computing Parameters for $\{8, 3\}$, Genus 2). For $\{8, 3\}$ on genus-2:

$$F = \frac{4 \cdot 3 \cdot (2 - 1)}{8 \cdot 3 - 2 \cdot 8 - 2 \cdot 3} = \frac{12}{24 - 16 - 6} = \frac{12}{2} = 6, \quad (11)$$

$$E = \frac{8 \cdot 6}{2} = 24, \quad V = \frac{8 \cdot 6}{3} = 16. \quad (12)$$

Verification: $V - E + F = 16 - 24 + 6 = -2 = 2 - 2(2)$. \checkmark

2.2.5 Asymptotic Scaling

The distinction between Euclidean and hyperbolic geometry affects quantum code parameters. In Euclidean geometry, area grows polynomially with radius ($A \sim r^2$), while in hyperbolic geometry, area grows exponentially ($A \sim e^r$).

Proposition 2 (Euclidean Scaling). For surface codes on Euclidean tessellations (e.g., the square lattice $\{4, 4\}$):

$$n = \Theta(d^2), \quad k = \Theta(1), \quad \frac{k}{n} = \Theta(1/n) \rightarrow 0. \quad (13)$$

The encoding rate vanishes as code size increases.

Theorem 2 (Hyperbolic Scaling). For hyperbolic surface codes with n physical qubits [10]:

$$\frac{k}{n} = \Theta(1) \quad (\text{constant rate}), \quad d = \Theta(\log n) \quad (\text{logarithmic distance}). \quad (14)$$

For edge-based CSS codes on $\{p, q\}$ tessellations, the asymptotic rate is $1 - 2/p - 2/q$ [10]. Fine-graining (Section 3.2) improves the distance scaling to $d = O(\sqrt{n})$ at fixed k . The resulting codes are termed semi-hyperbolic.

The logarithmic distance follows from systolic geometry: the systole (shortest non-contractible loop) of a hyperbolic surface of genus g is at most $4 \log g + O(1)$, and since $g \sim n$ for hyperbolic codes, $d = O(\log n)$ [17]. Figures 1–3 illustrate three hyperbolic tessellations in the Poincaré disk model.

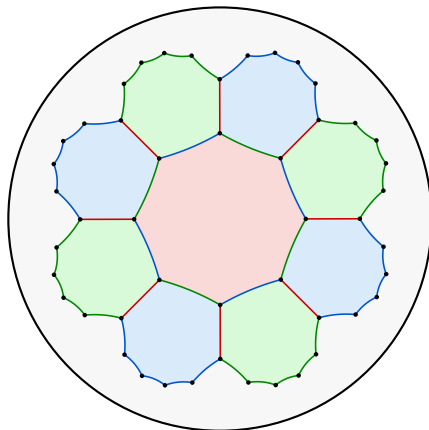


Figure 1: The $\{8, 3\}$ tessellation of the hyperbolic plane in the Poincaré disk model. Each face is a regular octagon with three faces meeting at every vertex.

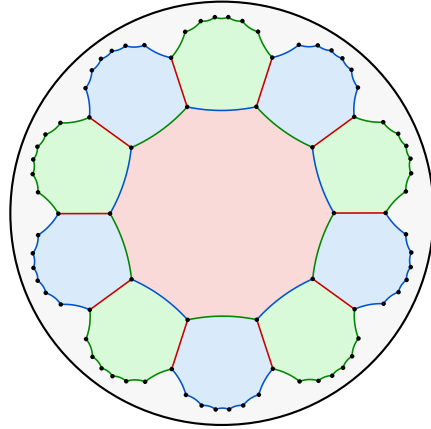


Figure 2: The $\{10, 3\}$ tessellation. Each face is a regular decagon.

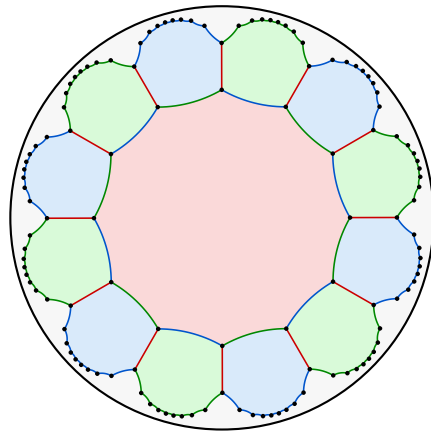


Figure 3: The $\{12, 3\}$ tessellation. Each face is a regular dodecagon. The exponential shrinking of faces toward the disk boundary reflects the negative curvature of the hyperbolic plane.

2.3 Hyperbolic Surface Codes

For CSS surface codes on tessellations, qubits are placed on edges with stabilizers associated with faces and vertices. We write \mathcal{S} for the stabilizer group and use S_f, S_v for individual stabilizer operators (elements of \mathcal{S}).

Definition 7 (Face and Vertex Stabilizers). A CSS surface code on a $\{p, q\}$ tessellation places one physical qubit per edge, so $n = E$. For each face f , define

$$S_f^X = \prod_{e \in \partial f} X_e \quad (\text{weight } p). \quad (15)$$

For each vertex v , define

$$S_v^Z = \prod_{e \in \text{star}(v)} Z_e \quad (\text{weight } q). \quad (16)$$

Proposition 3 (Number of Logical Qubits). For a surface code on a genus- g surface with V vertices, E edges, and F faces:

$$k = E - (F - 1) - (V - 1) = E - F - V + 2 = 2g, \quad (17)$$

using the Euler characteristic $\chi = V - E + F = 2 - 2g$. The F face stabilizers satisfy one linear dependency ($\prod_f S_f^X = I$) and therefore have rank $F - 1$. The V vertex stabilizers satisfy one dependency ($\prod_v S_v^Z = I$) and have rank $V - 1$ [10].

For the $\{p, 3\}$ tessellations studied here, each vertex has degree 3. The vertex stabilizers (Z -type) therefore have weight 3, and the face stabilizers (X -type) have weight p for $p \in \{8, 10, 12\}$.

3 Methods

3.1 Code Construction

3.1.1 Wythoff Construction and Triangle Groups

The Wythoff kaleidoscopic construction generates tessellations from reflections across the sides of a fundamental triangle [13]. The triangle group $\Delta(p, q, r)$ has presentation:

$$\Delta(p, q, r) = \langle a, b, c \mid a^2 = b^2 = c^2 = (ab)^r = (bc)^q = (ca)^p = e \rangle, \quad (18)$$

where a, b, c are reflections across three sides of a triangle with interior angles $\pi/p, \pi/q, \pi/r$. For a $\{p, q\}$ tessellation, we use $\Delta(p, q, 2)$, which acts on the hyperbolic plane when $1/p + 1/q + 1/2 < 1$.

A flag in the tessellation is an incident triple (vertex, edge, face). The triangle group acts simply transitively on flags, so each element of $\Delta(p, q, r)$ corresponds to exactly one flag. Vertices, edges, and faces are identified with orbits of flags under stabilizer subgroups generated by pairs of reflections.

For computation, we use the rotation subgroup $\Delta^+(p, q, 2) = \langle \alpha, \beta, \gamma \mid \alpha^2 = \beta^q = \gamma^p = \alpha\beta\gamma = e \rangle$, where $\alpha = ab, \beta = bc, \gamma = ca$ are rotations around edge midpoints, vertices, and face centers respectively. In the rotation subgroup, vertices are orbits under $\langle \beta \rangle$, edges are orbits under $\langle \alpha \rangle$, and faces are orbits under $\langle \gamma \rangle$.

3.1.2 LINS Algorithm and Face 3-Coloring

The Low-Index Normal Subgroups (LINS) algorithm enumerates finite-index normal subgroups of finitely presented groups. We use the GAP implementation [14] with the LINS package to enumerate subgroups of $\Delta^+(p, 3, 2)$. For each normal subgroup N with index i , the quotient Δ^+/N acts on a closed surface with $V = i/3$ vertices (since each vertex stabilizer has order 3). We filter for subgroups with genus $g \geq 2$.

The coset table produced by Todd-Coxeter enumeration encodes the graph adjacency. Geometric coordinates in the Poincaré disk are computed separately.

For $\{p, 3\}$ tessellations constructed via the Wythoff method, the faces admit a 3-coloring from the flag structure [13]. Each edge inherits its color as the complement of its two adjacent face colors:

$$\text{color}(e) = 3 - \text{color}(f_1) - \text{color}(f_2), \quad (19)$$

where f_1, f_2 are the faces incident to edge e and colors are labeled $\{0, 1, 2\}$.

3.1.3 Code Parameters

We construct 14 codes across the $\{8, 3\}$, $\{10, 3\}$, and $\{12, 3\}$ families. Table 1 lists the 6 $\{8, 3\}$ codes; the remaining 8 codes are in Appendix A. Each code is named HV after its vertex count V (so $n = 3V/2$ physical qubits for $\{p, 3\}$ tessellations). The code distance $d = \min(d_X, d_Z)$ is computed via integer linear programming (ILP), where d_X is the minimum weight of a non-trivial cycle and d_Z is the minimum weight of a non-trivial cocycle. Codes with $d = 2$ are omitted.

3.2 Fine-Graining

3.2.1 Procedure

The fine-graining procedure subdivides each triangle in the dual lattice into f^2 smaller triangles by inserting $f - 1$ vertices along each edge and $(f - 1)(f - 2)/2$ interior vertices per face. For a base code with parameters $[[n, k, d]]$, fine-graining with parameter f produces a code with:

$$n' = f^2 \cdot n, \quad k' = k. \quad (20)$$

The genus and number of logical qubits remain unchanged because fine-graining is a topological refinement that preserves the surface structure. The distance of the fine-grained code satisfies $d' \geq f \cdot d$; the values in Table 5 are computed independently by integer linear programming. The encoding rate $k/n' = k/(f^2 n)$ decreases quadratically with f . Fine-graining thus trades rate for distance.

3.2.2 Geometric Construction

For codes derived from hyperbolic tessellations, fine-graining must respect the hyperbolic metric. New vertices along edges are placed at hyperbolic geodesic midpoints using Möbius transformations in the Poincaré disk model.

Given two points $z_1, z_2 \in \mathbb{D}$, the geodesic midpoint is computed by:

1. Map z_1 to the origin via the isometry $\phi(z) = (z - z_1)/(1 - \bar{z}_1 z)$.
2. Find the hyperbolic midpoint along the radial geodesic: $w = \phi(z_2)/(1 + \sqrt{1 - |\phi(z_2)|^2})$.
3. Map back via $\phi^{-1}(w) = (w + z_1)/(1 + \bar{z}_1 w)$.

Interior vertices are placed using hyperbolic barycentric interpolation within each triangle. This procedure ensures that the subdivided lattice inherits the correct topology from the base tessellation.

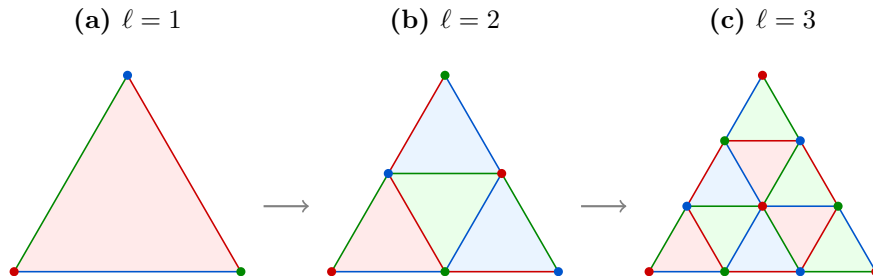


Figure 4: Fine-graining a single dual triangle. Each triangle connects three face centers with distinct colors (red, green, blue). Vertex colors are assigned by barycentric interpolation modulo 3. Edge colors follow the complement rule. (a) At $\ell = 1$, one triangle with three vertices. (b) At $\ell = 2$, the triangle subdivides into 4 smaller triangles with 6 vertices. (c) At $\ell = 3$, subdivision yields 9 triangles with 10 vertices. Each small triangle in the dual corresponds to a vertex in the fine-grained primal lattice.

3.2.3 Color Inheritance

For the CSS codes studied here, the fine-grained lattice inherits a canonical edge coloring from the base tessellation’s face 3-coloring. For subdivision parameter f , vertices at grid position (i, j) within a triangle with corner colors (c_A, c_B, c_C) receive color:

$$c(i, j) = c_A + i \cdot (c_C - c_A) + j \cdot (c_B - c_A) \pmod{3}. \quad (21)$$

3.3 Syndrome Extraction Circuit

Each syndrome extraction round measures all Z -stabilizers and X -stabilizers via ancilla qubits and CX (CNOT) gates. For a $\{p, 3\}$ code with n data qubits, one ancilla is allocated per stabilizer generator: one per vertex (Z -type, weight 3) and one per face (X -type, weight p).

The circuit for one round proceeds as follows:

1. Reset all ancilla qubits in $|0\rangle$.
2. Apply Hadamard to X -ancillas to prepare $|+\rangle$.
3. Apply CX gates between data qubits and ancillas. For Z -checks, data qubits are controls and the Z -ancilla is the target. For X -checks, the X -ancilla is the control and data qubits are targets.
4. Apply Hadamard to X -ancillas to return them to the Z basis.
5. Measure all ancillas in the Z basis.

Two data qubits that share a stabilizer cannot interact with the same ancilla simultaneously. The CX gates are scheduled into conflict-free layers. The Z -checks (weight 3, on vertices) are batched into 2 groups via bipartite coloring of the vertex conflict graph. The X -checks (weight p , on faces) are batched into 3 groups via the face 3-coloring inherited from the tessellation. Within

each batch, the CX gates for each stabilizer step occupy a single layer. The total number of CX layers per round is $2 \times 3 + 3 \times p$ (6 layers for Z -checks, $3p$ layers for X -checks).

The experiment is an X -memory test. All data qubits are initialized in $|+\rangle$, $T = d$ syndrome extraction rounds are performed, and data qubits are measured in the X basis. Detectors compare consecutive syndrome measurements. Boundary detectors compare the first (last) syndrome round to the initialization (final measurement) outcomes. The circuit tracks logical X observables throughout. We simulate circuits in Stim [18] and decode with PyMatching [19, 20].

3.4 Pauli Noise Model

Under the Pauli noise model, two-qubit depolarizing noise of strength p acts after every CX gate: each of the 15 non-identity two-qubit Paulis is applied with probability $p/15$. An X error of probability p acts after each ancilla reset and before each ancilla measurement. Single-qubit depolarizing noise of strength p acts after each Hadamard gate. This matches the standard circuit-level depolarizing model [7].

3.5 Erasure Noise Model

An erasure error occurs when a qubit’s state is lost but the loss event is detected. Erasure thresholds are higher than Pauli thresholds because the decoder can restrict its search to erased locations. We adopt the circuit-level erasure model of Chang et al. [7], built on the erasure qubit framework of Kubica et al. [6], parameterized by the total gate error probability p and the erasure fraction $R_e \in [0, 1]$. Each CX gate experiences one of three outcomes, mutually exclusively:

1. With probability $R_e \cdot p$, the gate is *flagged*: both output qubits are reset to a random state (maximally mixed), and the decoder is notified (aware decoding). On the decoding graph, flagged gates contribute edges with weight zero, encoding the prior knowledge that these locations contain errors.
2. With probability $(1 - R_e) \cdot p$, an undetected Pauli error from $\{I, X, Y, Z\}^{\otimes 2} \setminus \{II\}$ is applied uniformly at random (probability $p_p/15$ each, where $p_p = (1 - R_e) \cdot p$). These contribute standard log-likelihood-weighted edges.
3. With probability $1 - p$, the gate is noiseless.

At $R_e = 0$ the model reduces to standard depolarizing noise. At $R_e = 1$ all errors are detected. For each shot, the specific erasure pattern is sampled and a per-shot detector error model is constructed: flagged gates contribute weight-zero edges while unflagged gates contribute edges at standard depolarizing weights. The decoder operates on this per-shot graph. We simulate at $R_e \in \{0, 0.52, 0.71, 0.91, 1.0\}$, matching Chang et al.’s experimentally motivated values.

At temporal resolution $\eta = 1$, all erasures are detected immediately after the gate, before they propagate through subsequent operations. At $\eta = 1$, three of Chang et al.’s four noise models coincide [7]; only the tailored spatially perfect model differs, because the leaked qubit’s error type (X or Z) is determined by the gate type (CX or CZ), providing additional information to the decoder.

For aware decoding, the per-shot approach is more expensive than batch Pauli decoding. We use 3000 shots per (p, R_e, code) configuration.

3.6 Phenomenological Noise Model

We simulate the phenomenological noise model of Dennis et al. [8]: independent X errors, Z errors, and syndrome bit-flips each occur with probability p . We decode with MWPM via PyMatching.

3.7 Decoder

We decode X -type and Z -type errors independently using separate decoding graphs, following Chang et al. [7]. For CSS codes with parity-check matrices H_X and H_Z , the X -decoding graph is built from the X -stabilizer syndrome (face detectors), and the Z -decoding graph from the Z -stabilizer syndrome (vertex detectors). Each graph contains only the detectors of the corresponding type; error mechanisms that trigger detectors of both types are projected onto each graph independently.

For $\{p, 3\}$ tessellations, the X -decoding graph is strictly a graph (no hyperedges): a single Z error on a data qubit (edge) flips exactly two adjacent face stabilizers, and a measurement error on an X -ancilla flips two temporal detectors. No single circuit fault produces three or more X -type detector symptoms. The same holds for the Z -decoding graph by duality. This structural property ensures that minimum-weight matching and Union-Find decoders operate without information loss from hyperedge decomposition.

We use a weighted Union-Find decoder [23, 24] on each decoding graph. Union-Find runs in nearly linear time and accommodates the non-uniform edge weights that arise from erasure-aware decoding: flagged (erased) edges have weight zero, while unflagged edges carry standard log-likelihood weights. The weighted variant [24] grows clusters at rates inversely proportional to their boundary edge weights, providing an approximation to minimum-weight matching.

3.8 Threshold Estimates

For each code and noise model, we sweep over a range of physical error rates and compute the per-observable logical error rate, averaged across the k logical qubits. We use $T = d = \min(d_X, d_Z)$ syndrome rounds (Table 2). We define the pseudothreshold p^* as the physical error rate at which the per-cycle logical error rate $p_L = 1 - (1 - P_L)^{1/T}$ equals $k p$, interpolated linearly between adjacent data points; this is the break-even point where the encoded block performs as well as k unencoded qubits. When p_L remains below $k p$ throughout the tested range, we report $p^* > 5\%$. For scaling families with fixed k (Table 6), we estimate family thresholds from per-observable crossing points between consecutive code sizes. These results use MWPM via PyMatching [19, 20].

For the Chang et al. erasure analysis (Section 4.1.1), we instead use the quadratic expansion method of Wang et al. [25]:

$$P_L(p, d) = A + B x + C x^2, \quad x = (p - p_{\text{th}}) d^{1/\nu},$$

fitted simultaneously over all code sizes and error rates, yielding the threshold p_{th} and critical exponent ν . These results use the weighted Union-Find decoder (Section 3.7) on the X -decoding graph.

4 Results

4.1 Base Code Results

Table 1 lists the parameters of the 6 $\{8, 3\}$ base codes.

Table 1: Parameters of the 6 $\{8, 3\}$ hyperbolic surface codes. V is the number of vertices (= number of Z -stabilizers), $n = E$ is the number of physical qubits (edges), $k = 2g$ is the number of logical qubits, and $d = \min(d_X, d_Z)$ is the code distance computed via ILP. All codes are constructed via the Wythoff kaleidoscopic construction with the LINS algorithm (Section 3.2). Parameters for the $\{10, 3\}$ and $\{12, 3\}$ families are in Appendix A.

Code	V	n	k	d	k/n	Source
H32	32	48	6	3	12.5%	[14]
H64	64	96	10	4	10.4%	[14]
H144 _{8,3}	144	216	20	5	9.3%	[14]
H256	256	384	34	4	8.9%	[14]
H336 _{8,3}	336	504	44	6	8.7%	[14]
H432 _{8,3}	432	648	56	6	8.6%	[14]

Table 2 reports the Pauli and erasure pseudothresholds. The Pauli pseudothreshold increases with code size, from 0.24% (H64) to 0.49% (H432). Under erasure noise, three codes have measurable pseudothresholds of 3.3–3.7%; the larger codes exceed the tested range.

Table 2: Pauli and erasure pseudothresholds for the 6 $\{8, 3\}$ hyperbolic surface codes (2000 Pauli shots, 400 erasure shots per data point). The pseudothreshold p^* is defined as the solution of $p_L(p) = kp$, where $p_L = 1 - (1 - P_L)^{1/T}$ is the per-cycle logical error rate. Entries marked $>5\%$ indicate that $p_L < kp$ throughout the tested range. Results for the $\{10, 3\}$ and $\{12, 3\}$ families are in Appendix A.

Code	n	k	T	p^{*P}	p^{*E}
H32	48	6	3	$<0.2\%$	3.33%
H64	96	10	4	0.24%	3.66%
H144 _{8,3}	216	20	5	0.40%	3.63%
H256	384	34	4	0.42%	$>5\%$
H336 _{8,3}	504	44	6	0.47%	$>5\%$
H432 _{8,3}	648	56	6	0.49%	$>5\%$

4.1.1 Threshold vs. Erasure Fraction

We simulate the Bolza $\{8, 3\}$ semi-hyperbolic codes (H16-f2 through H16-f5, $k = 4$, $d_Z = 3, 4, 6, 7$, $n = 64\text{--}400$) under the two noise models that are distinct at $\eta = 1$ (Section 3.5) for erasure fractions $R_e \in \{0, 0.52, 0.71, 0.91, 1.0\}$. The number of syndrome extraction rounds is $T = d_X$ for each code, where d_X is the cycle distance ($d_X = 6, 8, 10, 14$ for $f = 2, 3, 4, 5$). We use 3000 shots per data point, the weighted Union-Find decoder on the X -decoding graph, and the Wang et al. quadratic expansion fit. These codes live on closed genus-2 surfaces with no spatial boundary. Table 3 reports the thresholds.

The threshold increases monotonically with R_e for both noise models. At $R_e = 1.0$, the threshold reaches 3.63% for Models 1–3 and 4.68% for Model 4. The erasure-to-Pauli ratios are $5.0\times$ (Models 1–3) and $6.5\times$ (Model 4). These ratios match the surface code values ($5.2\times$ and $6.8\times$) to within 5%, indicating that the erasure advantage transfers to hyperbolic codes at the same multiplicative factor. The absolute thresholds are 73% of the surface code values on average, reflecting that

Table 3: Thresholds for semi-hyperbolic $\{8, 3\}$ Bolza codes ($k = 4$, $d_Z = 3-7$, $n = 64-400$) under the Chang et al. noise model at $\eta = 1$. Models 1–3 coincide at $\eta = 1$. Wang-fit values from 3000 shots.

Model	R_e	Hyp. threshold	Surface threshold
Pauli baseline	0	0.72%	0.96%
Models 1–3	0.52	1.17%	1.61%
Models 1–3	0.71	1.51%	2.01%
Models 1–3	0.91	2.30%	3.10%
Models 1–3	1.0	3.63%	4.98%
Model 4	0.52	1.26%	1.65%
Model 4	0.71	1.70%	2.35%
Model 4	0.91	2.79%	3.79%
Model 4	1.0	4.68%	6.54%

hyperbolic codes encode $k = 4$ logical qubits with rate $k/n > 0$, leaving less redundancy per logical qubit than the $k = 1$ surface code.

Figure 5 plots the threshold against R_e for both code families and noise models. The Model 4 curve lies above Models 1–3 at each R_e . The gap widens with R_e : at $R_e = 0.52$, Model 4 is 8% higher; at $R_e = 1.0$, it is 29% higher. This is consistent with Chang et al.’s observation that the restricted error set $\mathcal{E}_{\text{tail}}$ provides the decoder with the Pauli type of the error on the leaked qubit, reducing the number of edges that are set to low weight on each decoding graph.

Figure 6 shows the per-observable logical error rate at $R_e = 0$ (Pauli baseline) for the four Bolza code sizes; the curves cross between $p = 0.7\%$ and $p = 0.8\%$, consistent with the Wang-fit threshold of 0.72%. Table 4 reports any-logical error rates under phenomenological noise. Within the $\{8, 3\}$ family, the any-logical rates for larger codes are lower at $p \leq 1\%$, suggesting a threshold near $p \approx 1-2\%$.

Table 4: Any-logical error rates (%) for $\{8, 3\}$ base codes under phenomenological noise (5000 shots). A trial fails if any of the k logical qubits is corrupted. Results for other families are in Appendix A.

Code	n	k	0.5%	1%	2%	3%	5%
H32	48	6	0.7	3.6	14.4	29.2	54.4
H64	96	10	1.0	4.4	18.1	36.1	69.5
H144	216	20	0.6	4.2	21.4	49.3	89.6
H432	648	56	0.4	4.6	33.8	76.4	99.8

4.2 Fine-Grained Code Results

Semi-hyperbolic codes [13] are obtained by fine-graining (Section 3.2), which increases n and d while preserving k . The resulting codes interpolate between hyperbolic ($d = O(\log n)$) and Euclidean ($d = O(\sqrt{n})$) distance scaling. Table 5 shows pseudothresholds for the $\{8, 3\}$ fine-grained codes; within each family, both pseudothresholds improve with refinement level.

The H16 Bolza family ($k = 4$) extends to $f = 4$ ($d = 8$) and reaches Pauli 0.63% and erasure 4.40%. The H64-f2 code ($k = 10$, $d = 8$) achieves Pauli 0.58% and erasure 4.10%.

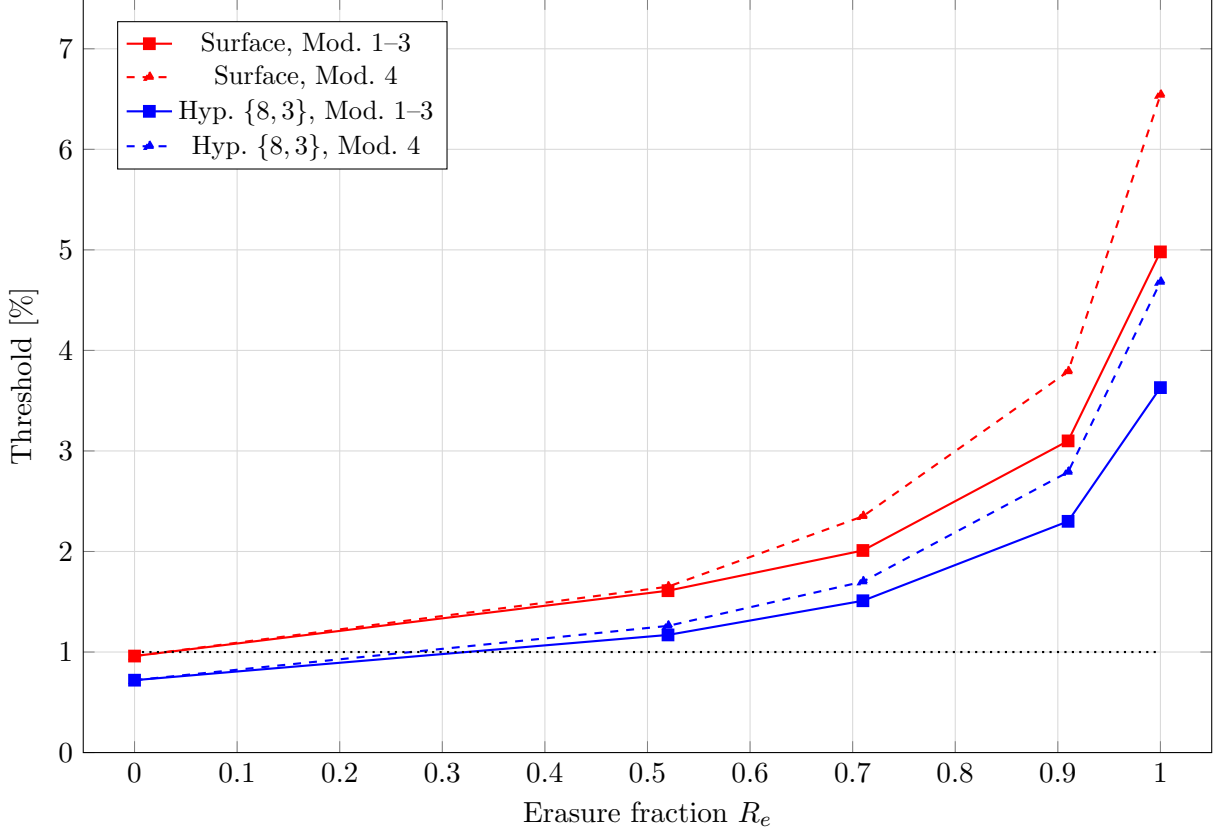


Figure 5: Threshold vs. erasure fraction R_e at $\eta = 1$ for the surface code ($d = 9-15$, $k = 1$) and the semi-hyperbolic $\{8, 3\}$ Bolza codes ($d_Z = 3-7$, $k = 4$). Solid lines: Models 1-3 (general Pauli, spatially imperfect). Dashed lines: Model 4 (tailored Pauli, spatially perfect). The dotted black line marks the Pauli threshold of Chang et al. [7].

Fine-grained codes derived from the same base code form scaling families with fixed k and increasing distance. Table 6 reports the per-observable family threshold for the Bolza family. At $R_e = 1$ (Models 1-3), the erasure-to-Pauli ratio of $5.3\times$ is comparable to the $5.2\times$ reported by Chang et al. for the planar surface code [7]. The Pauli family threshold (0.62%) is higher than the base code family threshold (0.53%), reflecting the larger distances achieved by fine-graining. Figure 7 shows the per-observable logical error rates under both noise models; the curves cross near $p \approx 0.6\%$ (Pauli) and $\varepsilon \approx 4\%$ (erasure).

Tables 7 and 8 report phenomenological error rates and compare fine-grained codes against base codes at matched qubit counts, illustrating the rate-distance trade-off.

4.3 Statistical Uncertainty

All error rates reported in this paper are Monte Carlo estimates from finite samples. For an observed any-logical error rate \hat{P}_L from N independent shots, the standard error is

$$\sigma = \sqrt{\frac{\hat{P}_L(1 - \hat{P}_L)}{N}}.$$

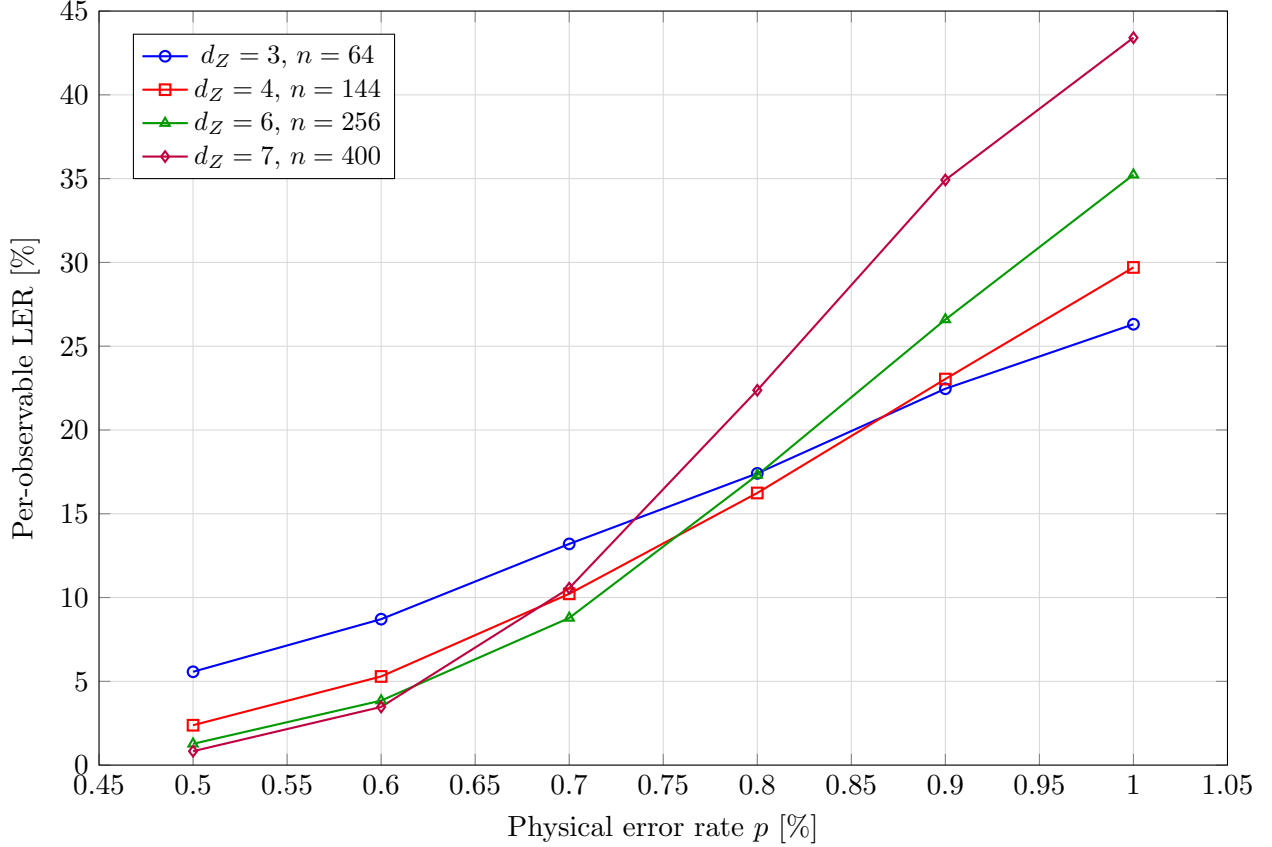


Figure 6: Per-observable logical error rate vs. physical error rate at $R_e = 0$ (Pauli baseline) for the semi-hyperbolic $\{8, 3\}$ Bolza codes ($k = 4$). The curves cross near $p = 0.7\%$, consistent with the Wang-fit threshold of 0.72% . All data: 3000 shots, weighted Union-Find decoder.

The Pauli simulations use $N = 2000$ shots for base codes and $N = 1000$ for fine-grained codes. At a representative error rate of $\hat{P}_L = 5\%$, the standard error is 0.49% ($N = 2000$) or 0.69% ($N = 1000$). The erasure simulations use $N = 400$ shots for base codes and $N = 200$ for fine-grained codes; the corresponding standard errors at $\hat{P}_L = 5\%$ are 1.09% and 1.54% . The phenomenological simulations use $N = 5000$ shots (standard error 0.31% at $\hat{P}_L = 5\%$).

Pseudothreshold estimates inherit uncertainty from the interpolation between adjacent data points. For error rates near $\hat{P}_L = 0$ or $\hat{P}_L \approx 1$, the relative precision is high. Near the crossing point, where $\hat{P}_L \approx 10\text{--}30\%$, the standard error is $\sim 0.7\text{--}1.0\%$ (Pauli) or $\sim 1.5\text{--}2.3\%$ (erasure).

Table 5: Pseudothresholds for the $\{8, 3\}$ semi-hyperbolic (fine-grained) codes with verified distances (1000 Pauli shots, 200 erasure shots per data point). The refinement level f indicates the subdivision factor. Base code results are included for comparison. The pseudothreshold p^* is the solution of $p_L = kp$. Results for the $\{10, 3\}$ and $\{12, 3\}$ fine-grained codes are in Appendix A.

Base	Level	n	k	d	T	p^{*P}	p^{*E}
H16 _{8,3}	base	24	4	2	2	<0.2%	2.39%
	$f = 2$	96	4	4	4	0.38%	4.16%
	$f = 3$	216	4	6	6	0.61%	4.29%
	$f = 4$	384	4	8	8	0.63%	4.40%
H64 _{8,3}	$f = 2$	384	10	8	8	0.58%	4.10%

Table 6: Fine-grained family threshold for the Bolza $\{8, 3\}$ family from per-observable crossing-point analysis. The family consists of codes at increasing refinement levels with constant $k = 4$. N denotes the number of consecutive-pair crossings found. Results for the $\{10, 3\}$ and $\{12, 3\}$ fine-grained families are in Appendix A.

Family	k	p_{th}^P	N_P	p_{th}^E	N_E	Ratio
H16 $\{8, 3\}$	4	0.62%	2	3.28%	2	$5.3\times$

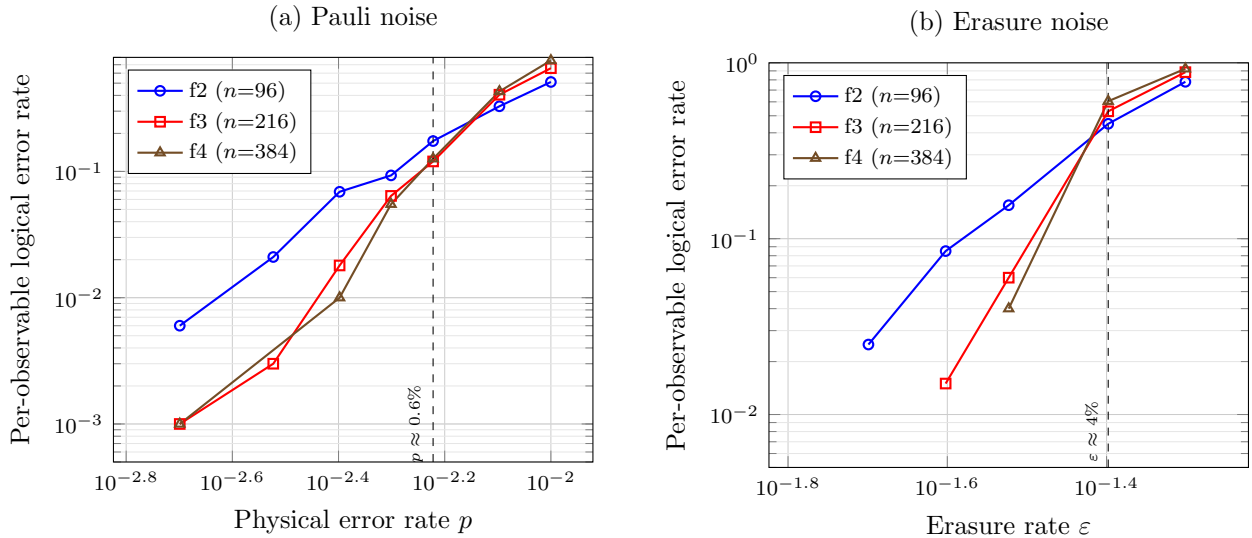


Figure 7: Per-observable logical error rate for the $\{8, 3\}$ H16 fine-grained family under (a) Pauli depolarizing noise (2000 shots) and (b) erasure noise (400 shots). Fine-graining levels f2 through f4 correspond to $n = 96, 216,$ and 384 physical qubits with $k = 4$ throughout. Under Pauli noise, curves cross near $p \approx 0.6\%$. Under erasure noise, curves cross near $\epsilon \approx 4\%$. Below threshold, larger codes achieve lower logical error rates.

Table 7: Any-logical error rates (%) for $\{8, 3\}$ fine-grained codes under phenomenological noise (5000 shots). A trial fails if any of the k logical qubits is corrupted. Results for other families are in Appendix A.

Base	Level	n	k	0.5%	1%	2%	3%	5%
H16 _{8,3}	$f = 2$	96	4	0.1	0.9	4.1	12.1	35.3
	$f = 3$	216	4	0.0	0.1	1.5	5.6	31.9

Table 8: Fine-grained vs base codes at matched qubit counts within the $\{8, 3\}$ family. The fine-grained codes trade encoding rate for distance.

Code	Type	n	k	d	k/n	p^{*P}	p^{*E}
H16-f3	fine	216	4	6	1.9%	0.61%	4.29%
H144 _{8,3}	base	216	20	5	9.3%	0.40%	3.63%
H16-f4	fine	384	4	8	1.0%	0.63%	4.40%
H64-f2	fine	384	10	8	2.6%	0.58%	4.10%
H256 _{8,3}	base	384	34	4	8.9%	0.42%	>5%

5 Discussion

5.1 Comparison with the Literature

Table 9 summarizes erasure and Pauli thresholds from the literature alongside our results.

Table 9: Erasure-to-Pauli threshold ratios from the literature and this work. “CC” denotes code capacity; “CL” denotes circuit-level. All entries are family thresholds (crossing points between code sizes). Our fine-grained values are from Table 6.

Code family	Reference	Noise	Pauli	Erasure	Ratio
Toric code	[8]	CC	10.9%	50.0%	4.6×
Planar surface	[7]	CL	1.0%	4.2–5.6%	4.2–5.6×
XZZX surface	[21]	CL	–	~4.3%	–
La-cross (HGP)	[22]	CL	–	4.0–4.6%	–
Hyp. Bolza fine-gr.	this work	CL	0.62%	3.28%	5.3×

At $R_e = 1$ (Models 1–3), the Bolza fine-grained family ratio (5.3×) matches the surface code value (5.2×).

5.2 Surface Code Validation

To validate our erasure simulation pipeline, we replicate the $\eta = 1$ thresholds of Chang et al. [7] for the unrotated surface code at distances $d = 9, 11, 13, 15$. At $\eta = 1$, Chang et al.’s four noise models reduce to two distinct models: Models 1–3 coincide, and only Model 4 (tailored, spatially perfect) differs. We sweep both models across $R_e \in \{0, 0.52, 0.71, 0.91, 1.0\}$, using the same weighted Union-Find decoder [24] and Wang et al. quadratic expansion fitting [25] with 3000 shots per data point. Table 10 compares our results.

Table 10: Validation against Chang et al. [7] at $\eta = 1$. At $\eta = 1$, three of Chang et al.’s four noise models coincide (Models 1–3); only Model 4 (tailored, spatially perfect) differs. Wang-fit thresholds from 3000 shots at $d = 9, 11, 13, 15$.

Config	R_e	Ours	Chang et al.	Diff.
Pauli baseline	0	0.96%	$1.00 \pm 0.01\%$	−4%
Models 1–3	0.52	1.61%	$1.60 \pm 0.02\%$	+1%
Models 1–3	0.71	2.01%	$2.08 \pm 0.02\%$	−3%
Models 1–3	0.91	3.10%	$3.12 \pm 0.04\%$	−1%
Models 1–3	1.0	4.98%	$5.09 \pm 0.02\%$	−2%
Model 4	0.52	1.65%	$1.71 \pm 0.02\%$	−4%
Model 4	0.71	2.35%	$2.33 \pm 0.03\%$	+1%
Model 4	0.91	3.79%	$3.80 \pm 0.03\%$	0%
Model 4	1.0	6.54%	$6.71 \pm 0.05\%$	−3%

All thresholds agree with Chang et al. to within 4% relative error. The threshold increases monotonically with R_e : from 0.96% at $R_e = 0$ (pure Pauli) to 4.98% at $R_e = 1.0$ (Models 1–3) and 6.54% (Model 4). Model 4 is 31% higher at $R_e = 1.0$ because the tailored error set $\mathcal{E}_{\text{tail}}$ restricts the leaked qubit to a single Pauli type (X or Z depending on the gate), so fewer edges are set to low weight on each decoding graph.

6 Conclusion

We constructed 14 hyperbolic CSS surface codes and 11 semi-hyperbolic codes across the $\{8, 3\}$, $\{10, 3\}$, and $\{12, 3\}$ tessellation families and simulated them under circuit-level erasure, circuit-level Pauli, and phenomenological noise. The main results focus on the $\{8, 3\}$ Bolza family, which forms a proper scaling family under fine-graining; results for the other families are in Appendix A.

The central trade-off is between encoding rate and error correction strength. Base codes have high encoding rates ($k/n = 8.6\text{--}12.5\%$) but low distances ($d = 3\text{--}6$), limiting their pseudothresholds. Fine-grained codes sacrifice rate (k/n decreases quadratically with the refinement level f) in exchange for higher distances ($d = 4\text{--}8$ at $f = 2\text{--}4$). Table 8 shows this trade-off: at $n = 384$, the $k = 4$ fine-grained code (H16-f4) reaches $p^{*E} = 4.4\%$, while the $k = 34$ base code (H256) exceeds the tested range entirely.

Under Chang et al.’s erasure noise model and Wang et al. quadratic expansion fitting, the Bolza family threshold reaches 3.6% (Models 1–3) and 4.7% (Model 4) at $R_e = 1$, with erasure-to-Pauli ratios ($5.0\times$ and $6.5\times$) matching the surface code values to within 5%. Per-observable crossing-point analysis at $R_e = 1$ (Models 1–3) independently yields a ratio of $5.3\times$, consistent with the surface code’s $5.2\times$. These results establish that the erasure advantage extends to hyperbolic codes.

Several directions remain open. Our fine-graining data cover $f \leq 4$; higher refinement levels would test whether the erasure pseudothreshold saturates near 4.4% or continues to increase. Extending the erasure analysis to Floquet-type measurement schedules on these same tessellations would connect the CSS results here to the broader hyperbolic Floquet literature [12, 13].

References

- [1] D. Gottesman, Stabilizer codes and quantum error correction, Ph.D. thesis, California Institute of Technology (1997); arXiv:quant-ph/9705052.
- [2] A. R. Calderbank and P. W. Shor, Good quantum error-correcting codes exist, *Phys. Rev. A* **54**, 1098–1106 (1996); arXiv:quant-ph/9512032.
- [3] A. M. Steane, Multiple-particle interference and quantum error correction, *Proc. Roy. Soc. Lond. A* **452**, 2551–2577 (1996); arXiv:quant-ph/9601029.
- [4] E. Knill, Quantum computing with realistically noisy devices, *Nature* **434**, 39–44 (2005).
- [5] Y. Wu, S. Kolkowitz, S. Puri, and J. D. Thompson, Erasure conversion for fault-tolerant quantum computing in alkaline earth Rydberg atom arrays, *Nat. Commun.* **13**, 4657 (2022); arXiv:2201.03540.
- [6] A. Kubica, A. Haim, Y. Vaknin, H. Levine, F. Brandao, and A. Retzker, Erasure qubits: Overcoming the T_1 limit in superconducting circuits, *Phys. Rev. X* **13**, 041022 (2023); arXiv:2208.05461.
- [7] K. Chang, S. Singh, J. Claes, K. Sahay, J. Teoh, and S. Puri, Surface code with imperfect erasure checks, arXiv:2408.00842 (2024).
- [8] E. Dennis, A. Kitaev, A. Landahl, and J. Preskill, Topological quantum memory, *J. Math. Phys.* **43**, 4452–4505 (2002).
- [9] T. M. Stace, S. D. Barrett, and A. C. Doherty, Thresholds for topological codes in the presence of loss, *Phys. Rev. Lett.* **102**, 200501 (2009).

- [10] N. P. Breuckmann and B. M. Terhal, Constructions and noise threshold of hyperbolic surface codes, *IEEE Trans. Inf. Theory* **62**, 3731–3744 (2016).
- [11] N. P. Breuckmann, C. Vuillot, E. Campbell, A. Krishna, and B. M. Terhal, Hyperbolic and semi-hyperbolic surface codes for quantum storage, *Quantum Sci. Technol.* **2**, 035007 (2017); arXiv:1703.00590.
- [12] A. Fahimniya, H. Dehghani, K. Bharti, S. Mathew, A. J. Kollár, A. V. Gorshkov, and M. J. Gullans, Fault-tolerant hyperbolic Floquet quantum error correcting codes, *Quantum* **9**, 1849 (2025); arXiv:2309.10033.
- [13] O. Higgott and N. P. Breuckmann, Constructions and performance of hyperbolic and semi-hyperbolic Floquet codes, *PRX Quantum* **5**, 040327 (2024); arXiv:2308.03750.
- [14] The GAP Group, GAP—Groups, Algorithms, and Programming, Version 4.12.2 (2022). <https://www.gap-system.org>
- [15] H. S. M. Coxeter, *Regular Polytopes*, 3rd ed., Dover, New York, 1973.
- [16] M. D. E. Conder and P. Dobcsányi, Trivalent symmetric graphs on up to 768 vertices, *J. Combin. Math. Combin. Comput.* **40**, 41–63 (2002).
- [17] L. Guth and A. Lubotzky, Quantum error-correcting codes and 4-dimensional arithmetic hyperbolic manifolds, *J. Math. Phys.* **55**, 082202 (2014); arXiv:1310.5555.
- [18] C. Gidney, Stim: A fast stabilizer circuit simulator, *Quantum* **5**, 497 (2021); arXiv:2103.02202.
- [19] O. Higgott, PyMatching: A Python package for decoding quantum codes with minimum-weight perfect matching, *ACM Trans. Quantum Comput.* **3**, 1–16 (2022); arXiv:2105.13082.
- [20] O. Higgott and C. Gidney, Sparse Blossom: correcting a million errors per core second with minimum-weight matching, *Quantum* **9**, 1600 (2025); arXiv:2303.15933.
- [21] K. Sahay, J. Jin, J. Claes, J. D. Thompson, and S. Puri, High-threshold codes for neutral-atom qubits with biased erasure errors, *Phys. Rev. X* **13**, 041013 (2023); arXiv:2302.03063.
- [22] L. Pecorari and G. Pupillo, Quantum low-density parity-check codes for erasure-biased atomic quantum processors, *Phys. Rev. A* **112**, 052417 (2025); arXiv:2502.20189.
- [23] N. Delfosse and N. H. Nickerson, Almost-linear time decoding algorithm for topological codes, *Quantum* **5**, 595 (2021); arXiv:1709.06218.
- [24] S. Huang, M. Newman, and K. R. Brown, Fault-tolerant weighted Union-Find decoding on the toric code, *Phys. Rev. A* **102**, 012419 (2020); arXiv:2004.04693.
- [25] C. Wang, J. Harrington, and J. Preskill, Confinement–Higgs transition in a disordered gauge theory and the accuracy threshold for quantum memory, *Ann. Phys.* **303**, 31–58 (2003); arXiv:quant-ph/0207088.

Table 11: Parameters of the $\{10, 3\}$ and $\{12, 3\}$ hyperbolic surface codes.

Family	Code	V	n	k	d	k/n	Source
$\{10, 3\}$	H50	50	75	12	3	16.0%	[14]
	H120	120	180	26	4	14.4%	[14]
	H250	250	375	52	4	13.9%	[14]
	H720	720	1080	146	4	13.5%	[14]
$\{12, 3\}$	H72	72	108	20	3	18.5%	[14]
	H96	96	144	26	3	18.1%	[14]
	H168	168	252	44	3	17.5%	[14]
	H312	312	468	80	3	17.1%	[14]

Table 12: Pauli and erasure pseudothresholds for $\{10, 3\}$ and $\{12, 3\}$ base codes (2000 Pauli shots, 400 erasure shots per data point).

Family	Code	n	k	T	p^{*P}	p^{*E}
$\{10, 3\}$	H50	75	12	3	0.11%	2.92%
	H120	180	26	4	0.20%	>5%
	H250	375	52	4	0.28%	>5%
	H720	1080	146	4	0.43%	>5%
$\{12, 3\}$	H72	108	20	3	0.07%	>5%
	H96	144	26	3	0.11%	>5%
	H168	252	44	3	0.12%	>5%
	H312	468	80	3	0.13%	>5%

A Results for $\{10, 3\}$ and $\{12, 3\}$ Families

Tables 11–13 report code parameters, pseudothresholds, and family thresholds for the $\{10, 3\}$ and $\{12, 3\}$ tessellation families. The $\{10, 3\}$ family achieves Pauli pseudothresholds of 0.11–0.43%. The $\{12, 3\}$ family has $d = 3$ for all four base codes regardless of size, and Pauli pseudothresholds of 0.07–0.13%.

Tables 14–15 report fine-grained pseudothresholds and family thresholds. The H50 family ($k = 12$) achieves an erasure-to-Pauli ratio of $5.2\times$; the H72 family ($k = 20$) achieves $4.5\times$.

Tables 16 and 17 report any-logical error rates under phenomenological noise.

Table 13: Family thresholds from per-observable crossing-point analysis for $\{10, 3\}$ and $\{12, 3\}$ base codes.

Family	p_{th}^{P}	N_{P}	p_{th}^{E}	N_{E}	Ratio
$\{10, 3\}$	0.59%	3	1.61%	2	$2.7\times$
$\{12, 3\}$	0.14%	1	0.55%	2	$3.9\times$

Table 14: Pseudothresholds for $\{10, 3\}$ and $\{12, 3\}$ fine-grained codes (1000 Pauli shots, 200 erasure shots per data point). Entries marked $>5\%$ indicate $p_L < kp$ throughout the tested range.

Base	Level	n	k	d	T	$p^{*\text{P}}$	$p^{*\text{E}}$
H50 _{10,3}	$f = 2$	300	12	6	6	0.52%	$>5\%$
	$f = 3$	675	12	9	9	0.62%	4.21%
H48 _{12,3}	$f = 2$	288	14	4	4	0.42%	4.73%
H72 _{12,3}	$f = 2$	432	20	6	6	0.51%	$>5\%$
	$f = 3$	972	20	9	9	0.61%	3.73%
H96 _{12,3}	$f = 2$	576	26	6	6	0.51%	$>5\%$
	$f = 3$	1296	26	9	9	0.62%	$>5\%$

Table 15: Fine-grained family thresholds for $\{10, 3\}$ and $\{12, 3\}$ families.

Family	k	p_{th}^{P}	N_{P}	p_{th}^{E}	N_{E}	Ratio
H50 $\{10, 3\}$	12	0.68%	2	3.53%	2	$5.2\times$
H72 $\{12, 3\}$	20	0.67%	1	3.04%	1	$4.5\times$

Table 16: Any-logical error rates (%) for $\{10, 3\}$ and $\{12, 3\}$ base codes under phenomenological noise (5000 shots).

Family	Code	n	k	0.5%	1%	2%	3%	5%
$\{10, 3\}$	H50	75	12	2.9	10.3	31.1	49.3	80.6
	H120	180	26	3.3	14.7	44.4	71.8	96.1
	H250	375	52	3.5	18.4	60.2	89.0	99.7
$\{12, 3\}$	H72	108	20	6.9	20.2	48.3	72.8	93.8
	H168	252	44	7.8	28.6	73.4	90.8	99.8
	H312	468	80	14.6	44.6	87.5	98.5	100.0

Table 17: Any-logical error rates (%) for $\{10, 3\}$ and $\{12, 3\}$ fine-grained codes under phenomenological noise (5000 shots).

Base	Level	n	k	0.5%	1%	2%	3%	5%
H50 _{10,3}	$f = 2$	300	12	0.0	0.3	6.0	21.6	70.1
	$f = 3$	675	12	0.0	0.0	1.0	9.0	62.1
H48 _{12,3}	$f = 2$	288	14	0.3	1.8	12.5	34.3	79.7
H72 _{12,3}	$f = 2$	432	20	0.1	0.9	10.5	36.5	88.9
	$f = 3$	972	20	0.0	0.0	1.7	14.3	81.7
H96 _{12,3}	$f = 2$	576	26	0.0	0.8	11.3	41.8	93.5
	$f = 3$	1296	26	0.0	0.0	1.3	16.9	88.1